APL Photonics

RESEARCH ARTICLE | OCTOBER 22 2024

Non-Hermitian mode management in periodically modulated waveguide amplifiers

Mohammad Nayeem Akhter ; Muriel Botey ; Ramon Herrero ; Kestutis Staliunas

APL Photonics 9, 106115 (2024)
https://doi.org/10.1063/5.0231659

Non-Hermitian mode management in periodically modulated waveguide amplifiers

Cite as: APL Photon. 9, 106115 (2024); doi: 10.1063/5.0231659
Submitted: 1 August 2024 • Accepted: 7 October 2024 •
Published Online: 22 October 2024

Mohammad Nayeem Akhter,[1] Muriel Botey,[1] Ramon Herrero,[1] and Kestutis Staliunas[1,2,3,a)]

AFFILIATIONS

[1] Department de Física, Universitat Politècnica de Catalunya, Rambla Sant Nebridi 22, 08222 Terrassa (Barcelona), Spain
[2] ICREA, Passeig Lluís Companys 23, 08010 Barcelona, Spain
[3] Faculty of Physics, Laser Research Center, Vilnius University, Sauletekio Ave. 10, 10223 Vilnius, Lithuania

[a)] **Author to whom correspondence should be addressed:** kestutis.staliunas@icrea.cat

ABSTRACT

We propose an efficient mode management scheme in active nonlinear multimode fibers based on non-Hermitian potentials in the longitudinal direction with an antisymmetric transverse profile. The proposal takes advantage of the nonlinear saturation toward particular mode configurations, which can be tuned by the non-Hermitian potential. We demonstrate flexible control of the beam profile within the parameter space of the applied potential with various possibilities, such as improving the beam quality by condensing photons to the lowest order Hermite mode, exciting higher order modes, or engineering a desired mode profile as a combination of modes. The effect is also analytically predicted using a mode-expansion approach, showing good agreement with the full model calculations based on the complex Ginzburg–Landau equation. This study was performed for 1D planar guiding structures, yet the results can be extended to 2D fibers and could be very useful in applications of fiber amplifiers and lasers.

I. INTRODUCTION

The emergence of non-Hermitian systems has impacted the field of photonics due to feasibility in the modulating of the refraction index and integrating gain and loss. This has enabled the design of artificial materials[1–4] with unprecedented features in extended systems[5–8] and also, in particular, in waveguide optics,[9–12] in this last case, generally relying only on transverse non-Hermitian modulations. Yet, proposals including non-Hermitian modulations in both transverse and longitudinal spatial directions have led to resonant linear mode conversion,[13,14] including a recent proposal in the context of graded index multimode optical fibers to achieve an efficient all optical linear mode-cleaning.[15,16]

Efficient schemes of transverse and longitudinal non-Hermitian modulations would be much desired in nonlinear multimode waveguides, or fiber amplifiers/lasers. Indeed, there is a rising demand for laser beams exhibiting different spatial profiles, driven by applications such as laser processing, lithography, medical procedures, and laboratory research.[17] Current beam-shaping techniques rely on a combination of refractive, diffractive, and reflective optical elements,[18–20] which generally relay, however, on a precise alignment of different optical elements. Therefore, a flexible fiber-integrated modal management scheme remains a challenge.

In the present paper, we propose a modal management scheme of active nonlinear systems such as multimode fiber (MMF) amplifiers. The proposal takes advantage of the multimode solutions in unmodulated parabolic nonlinear MMFs. The nonlinearity saturates the growing of the amplitudes of the modes, leading to particular mode configurations. Under the introduction of particular non-Hermitian modulations, it is possible to control the mode distribution and, therefore, the beam shape. For this purpose, we consider a harmonic non-Hermitian modulation, with a transverse antisymmetric profile, involving a modulation of both the refractive index and the gain/loss along a parabolic-index MMF amplifier. Figure 1(a) shows a possible implementation where index and gain/loss are periodically modulated in the longitudinal direction, while the snaking of the waveguide accounts for the antisymmetric transverse profile. The scheme could be intended to increase brightness to excite higher order modes or to flexibly manage the desired beam profile.

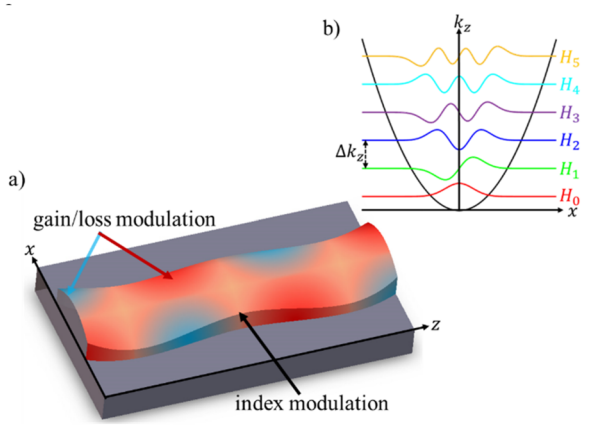

FIG. 1. (a) Schematic representation of a periodically modulated non-Hermitian 1D waveguide amplifier with a parabolic index profile. The index modulation along the propagation direction, z, is accounted by the fiber snaking, resulting in a transverse antisymmetric index perturbation. The gain/loss modulation is also antisymmetric in the transverse direction as indicated by the colors. (b) Lowest order Hermite modes of the 1D (unmodulated) parabolic waveguide with equispaced longitudinal wavenumbers $k_n = (n + \frac{1}{2})\Delta k_z$.

Therefore, we first perform a stability analysis of MMFs without modulation in order to determine the characteristic parameters for the single- and multi-mode operation. Then, we numerically explore the parameter space of the proposed non-Hermitian potential to find parameters allowing for different types of mode management. Finally, we also analytically explore the role of such non-Hermitian potential in 1D waveguides with a transverse antisymmetric profile considering the first three transverse modes system. Numerical simulations are in good agreement with the analytical predictions.

II. MODELLING THE NON-HERMITIAN WAVEGUIDE

The governing equation for light propagation along the active multimode fibers in CW or quasi-CW (long pulses) regimes in the presence of a complex potential is the complex Ginzburg–Landau equation (CGLE),

$$\frac{\partial A}{\partial z} = (1 + i\alpha)\left(p_0 e^{-gx^2} - |A|^2\right)A + id\nabla^2 A - icx^2 A + iV(x,z)A, \quad (1)$$

where $A(x,z)$ is the complex field amplitude envelope in the paraxial approximation, $p_0 e^{-gx^2}$ stands for the overall gain profile (be it a Raman gain, or a gain from doped ions) in transverse direction x, α is the self-focusing coefficient, c is the coefficient of parabolic background potential, and $V(x,z)$ is the profile of the perturbing complex-valued potential, as shown in Fig. 1(a). Such a non-Hermitian potential, $V(x,z)$, consists of two parts: the real part corresponding to index modulation (introduced by fiber snaking or thickness variation) and the imaginary part corresponding to the modulated gain/loss (introduced by absorption/scattering/transmission losses and gain by fiber doping).[16]

We consider the following antisymmetric perturbing potential:

$$V(x,z) = V(z)V(x) = [m_{re}\cos(qz) + im_{im}\cos(qz + \phi)]\left(\frac{x}{x_0}e^{-\frac{x^2}{x_0^2}}\right), \quad (2)$$

where m_{re} and m_{im} are the amplitude of the refractive index and gain/loss modulations, respectively, ϕ is the spatial shift between these two modulations, q is the modulation wavenumber, and x_0 is the half-width of the transverse spatial profile.

Without the complex potential $V(x,z)$, gain profiles and nonlinearities, the solutions of Eq. (1) are Hermite–Gauss eigenmodes of propagation in the background parabolic potential,

$$H_n = \frac{1}{\sqrt{\sqrt{\pi}2^n n! w_0}}\mathrm{H}_n(x/w_0)exp(-x^2/(2w_0^2)), \quad (3)$$

where $\mathrm{H}_n(x)$ are the Hermite polynomials, with n being the non-negative integer mode index and w_0 is the spot size of the fundamental mode. The corresponding mode propagation wavenumbers $k_n = (n + \frac{1}{2})\Delta k_z$ are equispaced with $\Delta k_z = 2\sqrt{cd}$. Thereby, due to this equidistant mode propagation constant, beams propagating in MMF exhibit a self-imaging with period $\zeta = 2\pi/\Delta k_z$.

III. RESULTS AND DISCUSSIONS

A. Stability analysis

We first perform the stability analysis of the system without the non-Hermitian modulation, $V(x,z) = 0$ and for the fundamental transverse mode. We consider a simple approximation of the system dynamics near the lowest transverse mode, H_0, and we assume an oscillatory Gaussian ansatz of the form[21]

$$A(x,z) = \sqrt{\rho(z)}e^{-\beta(z)x^2}, \quad (4)$$

with real-valued beam amplitude $\rho(z)$ and complex-valued beam waist parameter $\beta(z) = \beta_{re}(z) + i\beta_{im}(z)$. The evolution of these variables, as derived from Eq. (1), is governed by the system of ordinary differential equations,

$$\frac{d\beta_{re}}{dz} = -2\rho\beta_{re} + 8d\beta_{im}\beta_{re} + gp_0, \quad (5a)$$

$$\frac{d\beta_{im}}{dz} = -2\alpha\rho\beta_{re} + c - 4d\left(\beta_{re}^2 - \beta_{im}^2\right) + p_0 g\alpha, \quad (5b)$$

$$\frac{d\rho}{dz} = -2\rho^2 + 4d\beta_{im}\rho + 2p_0\rho. \quad (5c)$$

The stationary solution $(\beta_{re0}, \beta_{im0}, \rho_0)$ can be found analytically by equating $d\beta_{re,im}/dz$, $d\rho/dz = 0$, in the absence of modulation, $m_{re} = m_{im} = 0$. We perform linear stability analysis of the stationary solution by calculating the eigenvalues of the corresponding Jacobian matrix. Figure 2(a) shows the stability map calculated from the set of Eq. (5) in the parameters space of the system (α, g)—self-focusing coefficient and the gain profile. A Hopf bifurcation separates a stable region, where the real parts of all eigenvalues are negative, and an unstable region with two complex-conjugated eigenvalues with positive real parts. Propagation in these two regions respectively leads to a stable point or to periodic trajectory in the

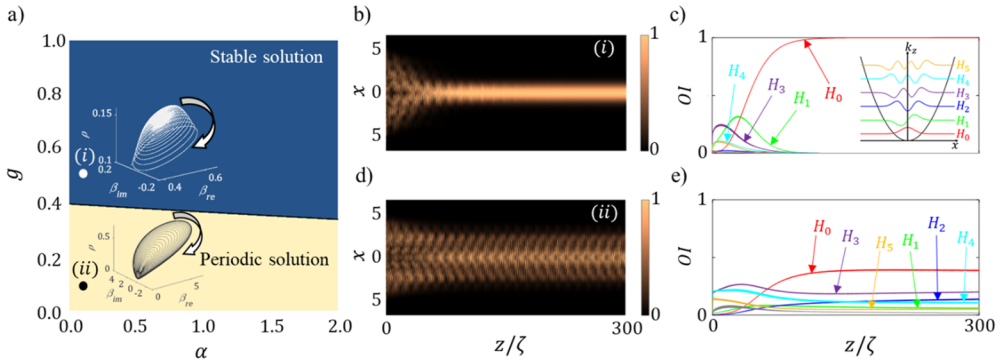

FIG. 2. (a) Stability map calculated form the set of Eq. (5) in the parameter space of (α, g). The insets of panel (a) correspond to phase space evolutions at points (i) (white dot) and (ii) (black dot). (b) and (d) Beam evolution and (c) and (e) corresponding evolution of the normalized mode projection, for the case (i) and (ii), respectively. The spatial coordinate z is normalized to the self-imaging period ζ. Other parameters used are $c = d = 1$.

phase space of $(\beta_{re}, \beta_{im}, \rho)$; see the insets of Fig. 2(a). In the first case, the system evolves to a stable point through damped oscillations; see inset (i), whereas inset (ii) depicts the evolution toward a periodic orbit. We also observe analogous behavior by numerical integration of Eq. (1), in the absence of the non-Hermitian potential. An incident multimodal beam experiences a different evolution upon propagation within the (α, g) parameter space. Within the stable range, any initial multimodal beam ends up in a mono-mode propagation of the lowest order mode H_0; see Fig. 2(b). It should be noted that the normalized mode projection to H_0 reaches 1, as shown in Fig. 2(c). Meanwhile, the unstable region in the Gaussian ansatz model corresponds to multimodal solutions of the full CGLE model. Indeed, Figs. 2(d) and 2(e) show the evolution of a beam within the multimodal range and its normalized mode projection, as calculated by the overlap integral (OI) of the total field on every H_n mode,

$$OI_n = \frac{|\int A \times H_n dx|^2}{\int |A|^2 dx \int |H_n|^2 dx}. \tag{6}$$

It is worth mentioning that H_0 is the only stable mono-mode solution for the unmodulated system observed upon integration of the full CGLE model with a similar boundary in the parameter space determined by the Hopf bifurcation for the simple Gaussian model. The second Hermite mode H_1 also shows partial stability in a range of the parameter space but only in the subspace of the odd Hermite modes.

In the following, we focus the study on the periodic (multimode) region (e.g.; $c = d = 1, g = \alpha = 0.1$) and explore how the antisymmetric non-Hermitian potential shapes the beam profile.

B. Direct integration

Next, we analyze the multimode non-Hermitian waveguide by direct integration of Eq. (1). We introduce the potential of Eq. (2) with an antisymmetric shape in x, the transverse direction, and integrate the field amplitude $A(x, z)$ using the split-step Fourier method.

In order to characterize the mode management, we calculate the relative intensity or mode projection as the overlap integral, Eq. (6), of the eigenmodes of the unmodulated system.

To assess the mode management and beam shaping, we first numerically explore the parameter space (ϕ, Q) for a fixed value of modulation amplitudes, m_{re}, m_{im}, where $Q = q/\Delta k_z$ is the spatial frequency of the non-Hermitian modulation normalized to the resonant frequency $q_{res} = \Delta k_z$. We propagate along the fiber an initially random beam and map the mode projections of the first six lower order modes, $H_n, n = 0, 1, \ldots, 5$, after a sufficiently long propagation distance, as shown in Fig. 3. Figure 3(a) shows the general map of all the calculated mode projections in the parameter space (ϕ, Q) and fixed values of the amplitudes, m_{re} and m_{im}, while the detailed relative intensities of the first six modes are shown in Fig. 3(b)–3(g). The insets of Fig. 3(a) show different beam shapes corresponding to particular positions within the map. Therefore, the fiber parameter determines the final transverse profile of the output beam and could be designed intended to beam-shape the input light. Interestingly, there are regions (in red) corresponding to $\pi/2 < \phi < 3\pi/2$, for modulation frequency below resonance, $Q < 1$ and $-\pi/2 < \phi < \pi/2$, for modulation frequency, $Q > 1$, where the projection of the lowest order mode, H_0, is maximal, reaching a mono-mode regime. It should be noted that there are regions in the parameter space where the overlap integral is 1, as shown in Fig. 3(b). This indicates that the non-Hermitian potential is shifting the mono-mode/multimode boundary shown in Fig. 2(a), as found in the stability analysis. Ranges where the relative intensity of H_0 are maximized could be used for all-optical mode-cleaning. Irrespective of the initial conditions, a beam propagating along the fiber would acquire a perfect Gaussian spatial profile, increasing the beam quality and brightness. In turn, Fig. 3(c) shows that mode H_1 is maximized in some ranges, coexisting with other modes. In the same way, mode H_2 is also maximized up to an almost 100% within the map (blue region) for a range of parameters corresponding to $\pi/2 < \phi < 3\pi/2$, above resonance and $-\pi/2 < \phi < \pi/2$, below resonance, as shown in Fig. 3(d). It should be noted from Figs. 3(e)–3(g) that modes H_3, H_4 and H_5 are also dominant in some regions, yet with lower relative integrals, hence in a multimode configuration.

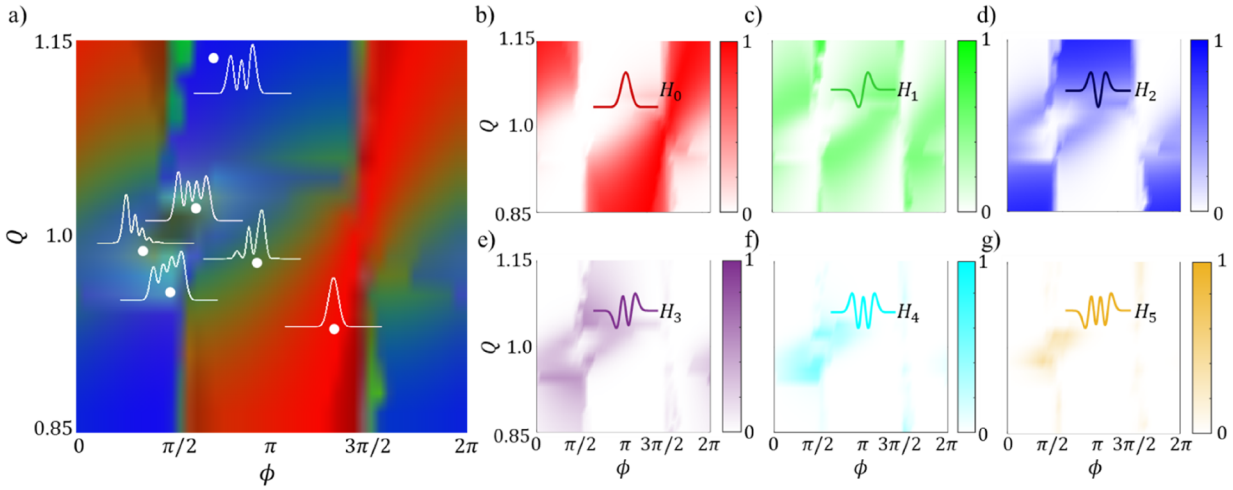

FIG. 3. (a) Overlapped map of the normalized mode projections, *OI*, of all the modes as calculated by Eq. (6), in the total field in the parameter space (ϕ, Q) for a fixed value of the modulation amplitudes, m_{re} and m_{im}, where relative intensity of every mode corresponds to one color: red to H_0, green to H_1, blue to H_2, violet to H_3, cyan to H_4, brown to H_5, and black to the rest of modes. The insets show different beam profiles corresponding to the white dots. Panels (b)–(g) depict the particular map of the first six modes, H_0–H_5, plotted as the intensity map, where the maximum corresponds to a mono-mode beam. The parameters used are $m_{re} = m_{im} = 0.6$; in addition, throughout this paper, we fix $g = \alpha = 0.1, c = d = 1$.

As an example of the proposed mode management by modulated non-Hermitian fibers, the mode cleaning regime is available in all the red region shown in Fig. 3(a). The evolution of the transverse spatial profile of the beam is shown in Fig. 4. We observe that the participation decreases in high modes in propagation along the fiber, while *OI* of the lowest order mode, H_0, increases asymptotically approaching to unity and reaching a mono-mode output. This effect is also evident from the inspection of intensity profile; see Fig. 4(b). The highly multimodal input distribution of the beam gradually evolves toward a bell-shaped transverse profile.

To quantitatively characterize the mode-cleaning, we calculate the evolution of the beam quality factor M^2. The inset of Fig. 4(a) clearly shows a significant reduction of the beam quality factor, as M^2 gradually approaches unity, acquiring an almost Gaussian profile.

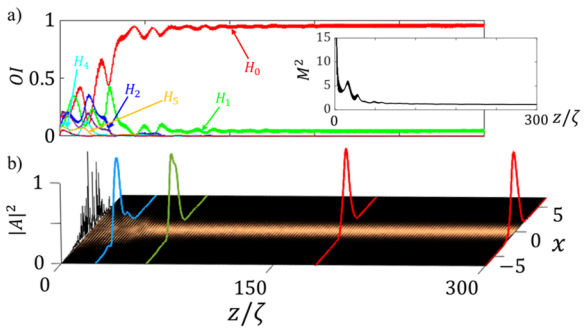

FIG. 4. (a) Relative mode intensity, *OI*, for an incident noisy beam, as a function of the propagation distance. The inset shows the evolution in the space of the beam quality factor. (b) Evolution in the propagation of the corresponding profiles depicted at particular distances, namely, $z = 1\zeta, 30\zeta, 70\zeta, 190\zeta$, and 300ζ. The parameters used are $m_{re} = m_{im} = 0.6$, $Q = 0.925$, $\phi = 4.42$.

IV. MODAL EXPANSION

In order to acquire a physical insight into the effect of the nonlinear multimode modulated fiber and analytically asses the interaction among modes for the modulated 1D case, we derive a coupled mode model, containing n transverse modes, using the standard mode expansion technique for the optical field $A(x,z)$,[22,23]

$$A(x,z) = \sum_{i=1}^{n} a_i(z) H_i(x). \tag{7}$$

Here, $a_i(z)$ stand for the z-dependent mode coefficients, and $H_i(x)$ is the set of orthonormal transverse Hermite modes, Eq. (3). The ansatz (7) is inserted into Eq. (1) to obtain the system of equations for the amplitudes of transverse modes, $a_i(z)$. The intensity term $|A|^2$ becomes

$$|A|^2 = \sum_{i,j=1}^{n} a_i a_j^* H_i H_j^*. \tag{8}$$

Inserting expansions (7) and (8) into Eq. (1), multiplying Eq. (1) by $H_i^*(x)$ and integrating over the transverse coordinate x, the following system of equations for the mode coefficients is obtained:

$$\frac{\partial a_i}{\partial z} = (1+i\alpha)\left(\sum_{j=1}^{n} P_{ji} a_j - \sum_{klj=1}^{n} G_{klji} a_k a_l^* a_j\right) + ik_i a_i + iV(z)\sum_{j=1}^{n} C_{ji} a_j, \tag{9}$$

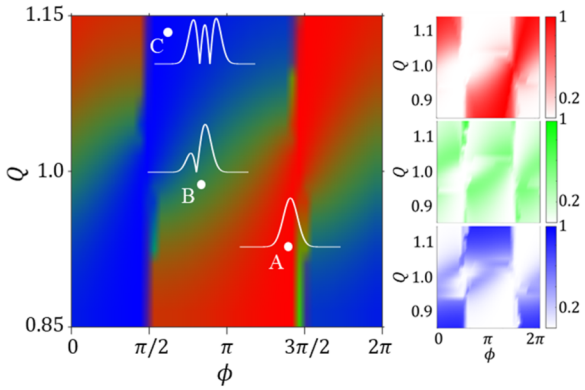

FIG. 5. RGB map of the normalized mode projections of the first three transverse modes, H_0 (red), H_1 (green), and H_2 (blue) in the total field, after a propagation distance $z = 1500\zeta$, in the parameter space of (ϕ, Q) for a fixed m_{re} and m_{im}. The insets display the different beam profiles corresponding to the white dots, labeled A, B, and C. The insets displayed on the right-hand side are analogous to Figs. 3(b)–3(d). The amplitude of the complex potential is the same as in Fig. 4: $m_{re} = m_{im} = 0.6$.

where $P_{ji} = \int p_0 e^{-gx^2} H_j H_i^* dx$, $G_{klji} = \int H_k H_l^* H_j H_i^* dx$ and $C_{ji} = \int x/x_0 e^{-x^2/x_0^2} H_j H_i^* dx$ are the matrix elements of the coupling between the transverse modes, arising from the different terms of Eq. (1), the gain profile, the nonlinear term, and the non-Hermitian potential, respectively, and k_i being the above-defined ith mode propagation wavenumber. Due to the different parities of the modes, some of the integrals are zero. Here, we numerically solve the system of Eq. (9) considering the three lowest transverse modes. The values of the non-zero coupling coefficients, for the case of three modes are included in Appendix A. We explore the parameter space of (ϕ, Q) for a fixed non-Hermitian potential, i.e., for constant amplitude values m_{re}, m_{im}, and map OI of each of the three modes after a sufficiently long propagation distance. The result is shown in Fig. 5, plotted as an RGB image, corresponding to the first three Hermite modes. Each color represents a different mode relative intensity: red corresponds to H_0, green corresponds to H_1, and blue corresponds to H_2. In accordance to the direct integration results, OI of the first mode, H_0, is maximum in a phase range (in red) corresponding to $\pi/2 < \phi < 3\pi/2$, for modulation frequency below resonance, $Q < 1$ and $-\pi/2 < \phi < \pi/2$, for modulation frequency above resonance, $Q > 1$, where OI reaches 1. Such phase range depends on the detuning. Exactly at resonance, $Q \simeq 1$, the mode-cleaning range squeezes and we retrieve the PT-symmetry condition for a phase delay of $3\pi/2$. Yet, off-resonance, mode cleaning occurs in a wider phase range, which increases with the detuning. In turn, such phase range broadens asymmetrically depending on the sign of the detuning, becoming more robust. Above resonance, the optimum phase ranges from $3\pi/2$ toward 0, while below resonance, it broadens toward π.

Inspecting OI of the third mode, H_2, the tendency is almost complementary to H_0; see the blue range on Fig. 5. Interestingly, the values of OI of mode H_1 correspond to the geometrical mean of OI of the modes H_0 and H_2, consistent with the eigenvectors obtained by simple linear analysis of the system; see Appendix B. The insets in Fig. 5(a) show the profiles of the beam amplitude for particular points on the map. The insets on the right-hand side of Fig. 5(a) are analogous to Figs. 3(b)–3(d), which demonstrate the agreement between the numerical and analytical calculations.

Finally, we show that irrespective of the initial conditions of the input beam, the system evolves toward the same final state, which only depends on the system parameters. No bistability has been found. We present an example of the evolution of the participations of the first three modes for three different non-Hermitian waveguides, corresponding to the three white dots shown in Fig. 5. Figures 6(a) and 6(c) show two examples, far from resonance, where the first and third modes, H_0 and H_2, become dominant after propagation along the fiber. In turn, Fig. 6(b) shows the evolution for a near-resonant modulation, where the second mode H_1 becomes

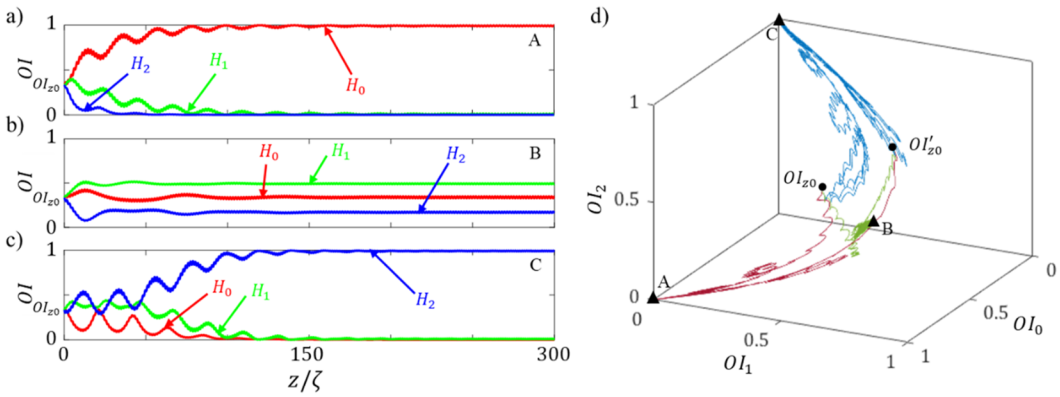

FIG. 6. Evolution of OI for the first three modes, along the propagation distance, toward the final states, for three different modulations: (a) $(\phi, Q) = (4.42, 0.925)$, (b) $(\phi, Q) = (2.85, 0.975)$, and (c) $(\phi, Q) = (1.85, 1.13)$, mapped in Fig. 5. (d) Phase space evolution of OI, for two different initial conditions with mode relative intensity distributions, OI_{z0}, being $OI_1 = OI_2 = OI_3 = 33.33\%$ and OI'_{z0} being $OI_1 = 6\%$, $OI_2 = OI_3 = 47\%$ for the above-mentioned modulations. The final states are labeled A, B, and C and marked with a triangle, and correspond to the points shown in Fig. 5. Other parameters used are same as those shown in Fig. 5.

dominant, but with a strong participation of modes H_0 and H_2. In all three cases, the final states (labeled *A, B*, and *C*) hold a final constant participation of the three modes, H_0, H_1, and H_2. It should be noted that the above-mentioned three cases have the same initial mode configuration, OI_{z0} shown in Fig. 6(d). The system leads to the same final stable stationary state starting from any initial condition. As an example, we show phase space evolutions from a second initial condition, OI'_{z0} shown in Fig. 6(d). Both the initial conditions are indicated by the two black dots in Fig. 6(d). It should be noted that the curves depicted with the same color in Fig. 6(d) correspond to the same non-Hermitian modulation, but are starting from different initial configurations and reaching the same final points A, B, and C marked with triangles.

We also perform additional calculations in order to see the effect of nonlinearity by varying the modulation amplitudes. We even compare the differences of the potential effects on simple linear and nonlinear systems; see Appendix B.

Finally, Appendix C provides an example of mode-shaping from an arbitrary noisy beam to a particular beam profile other than the Gaussian, the robustness of this mechanism for deformed parabolic potentials, and the effectiveness for a flat gain profile ($g = 0$) yet requiring higher modulation amplitudes.

V. CONCLUSIONS

We demonstrate significant mode control in active nonlinear parabolic index MMFs, broadly used in multimode fiber amplifiers and lasers, by applying harmonic non-Hermitian potentials in the longitudinal direction, with an antisymmetric transverse profile. We investigate the output mode profile in the parameter space of the applied non-Hermitian potential, showing flexible mode management. The nonlinearity helps the beam to be saturated in different shapes and does not allow the modes to grow exponentially. Depending on the phase shift between the gain/loss and index modulations and the detuning from resonance of the harmonic modulations, it is possible to manage the mode composition. Such selection of a desired profile could be very useful in the applications of fiber lasers. It is also possible to improve the beam quality, as the beam profile evolves toward the lowest order mode H_0, demonstrating efficient all-optical mode-cleaning. Alternatively, the participations of higher order modes may be increased reaching almost mono-mode propagation for H_2. Our calculation shed some light on the optimum phase shift between the quadrature of modulation. For mode cleaning, we note that exactly at resonance, such phase retrieves the conditions for PT-symmetry, being $3\pi/2$. However, detuning induces a broadening of the optimum phase range. Such broadening depends on the sign of the detuning. It broadens asymmetrically from $3\pi/2$, toward 0 above resonance and toward π below resonance.

The effect is also demonstrated analytically using the standard mode-expansion technique considering the first three Hermite modes. We see that the non-Hermitian potential shifts the mono-mode/multimode boundary of the solutions of the system. The analytical findings are in good agreement with the numerical integration of the full model (CGLE) calculations. This study was performed for 1D planar guiding structures, however, the effect can be generalized to 2D fibers.

The actual fabrication of the proposed non-Hermitian 1D waveguides could be achieved in both 1D and 2D configurations. Periodic index modulation is feasible through various nanofabrication techniques, yet gain/loss could be achieved introducing periodic distributed losses in a homogeneous active waveguide/fiber. In 1D waveguides, current lithographic techniques could be employed for fabrication.[12,24–26] Meanwhile, in 2D waveguides, achieving the necessary index and gain/loss modulation might involve techniques such as doping the fiber core[27,28] and introducing distributed absorption, scattering, or transmission losses.[29–31] These methods could potentially enable the realization of the desired properties in the waveguides.

This study is based on GRIN waveguides, with a parabolic index profile that supports the equidistant modes. However, deviations from perfect parabolic profile (and hence no strictly equidistant set of modes) are possible, as the effect is robust for any input beam and also works away from resonance.

An estimate of the required actual length of the waveguide to achieve a stable output is on the order of 20 cm, assuming realistic values for the non-Hermitian parabolic waveguide such as core radius, $r_c = 26\ \mu$m, core refractive index, $n_{co} = 1.47$, and cladding refractive index, $n_{\mathrm{cl}} = 1.457$.

ACKNOWLEDGMENTS

This work received funding from the Horizon 2020 program project MEFISTA (Project No 861152) and from the Spanish Ministry of Science, Innovation, and Universities (MICINN) under Project No. PID2022-138321NB-C21.

AUTHOR DECLARATIONS

Conflict of Interest

The authors have no conflicts to disclose.

Author Contributions

Mohammad Nayeem Akhter: Conceptualization (equal); Formal analysis (equal); Investigation (equal); Writing – original draft (equal); Writing – review & editing (equal). **Muriel Botey**: Conceptualization (equal); Formal analysis (equal); Investigation (equal); Supervision (equal); Writing – original draft (equal); Writing – review & editing (equal). **Ramon Herrero**: Conceptualization (equal); Formal analysis (equal); Investigation (equal); Supervision (equal); Writing – original draft (equal); Writing – review & editing (equal). **Kestutis Staliunas**: Conceptualization (equal); Formal analysis (equal); Investigation (equal); Supervision (equal); Writing – original draft (equal); Writing – review & editing (equal).

DATA AVAILABILITY

The data that support the findings of this study are available from the corresponding authors upon reasonable request.

APPENDIX A: COUPLING COEFFICIENTS FOR THREE-MODES MODEL

For reference, we list here the values of the non-zero integrals of Eq. (9): $P_{11} = 0.0949$, $P_{22} = 0.0849$, $P_{31} = -0.0071$, $P_{33} = 0.0748$,

$G_{1111} = 0.2502$, $G_{1113} = -0.1407$, $G_{1122} = 0.1989$, $G_{1133} = 0.1492$, $G_{1223} = 0.0703$, $G_{1333} = 0.0175$, $G_{2222} = 0.2984$, $G_{2233} = 0.1741$, $G_{3333} = 0.2549$, $C_{12} = 0.2532$, and $C_{23} = 0.2502$.

APPENDIX B: LINEAR VERSUS NONLINEAR SYSTEMS

Here, we demonstrate the difference between the effects of the non-Hermitian potential on the linear and nonlinear CGLE model. We derive an approximate simple coupling matrix for the three-mode case by considering coupled mode theory in the linear system as in Ref. 16. Basically, we remove the gain and the nonlinear terms from Eq. (1). The coupling matrix in this simple linear system is given by

$$\begin{pmatrix} -i\Delta q & im_+CC & 0 \\ im_-CC & 0 & im_+CC \\ 0 & im_-CC & i\Delta q \end{pmatrix}, \tag{B1}$$

where $\boldsymbol{\Delta q}$ is the difference between the applied non-Hermitian frequency and the resonance frequency, $\boldsymbol{m_+} = \boldsymbol{m_{re}} + \boldsymbol{im_{im}}e^{i\phi}$, $\boldsymbol{m_-} = \boldsymbol{m_{re}} + \boldsymbol{im_{im}}e^{-i\phi}$, and $\boldsymbol{CC}$ is the coupling coefficient between neighboring modes. As a simplification, we assume equal values for all the coupling coefficients. In this case also, we explore the parameter space of $(\phi, \boldsymbol{\Delta q})$ for different amplitudes of the non-Hermitian potential $(\boldsymbol{m_{re}}, \boldsymbol{m_{im}})$ in order to observe the differences between the linear and nonlinear system, in the presence of the non-Hermitian perturbation potential. We explore the effect of the nonlinearity and amplitude on the non-Hermitian potential by mapping the participation of each of the three modes ($\boldsymbol{H}_0$ in red, $\boldsymbol{H}_1$ in green, and $\boldsymbol{H}_2$ in blue) for both the linear and nonlinear systems. Such comparison is shown in Fig. 7. Figures 7(a), 7(c), and 7(d) show the calculation for the linear system by solving the matrix in Eq. (B1), for three different sets of amplitudes: $((\boldsymbol{m_{re}}, \boldsymbol{m_{im}}) = 0.6$, $((\boldsymbol{m_{re}}, \boldsymbol{m_{im}}) = 0.3$, and $((\boldsymbol{m_{re}}, \boldsymbol{m_{im}}) = 0.1$. For comparison, we repeat the calculations for the nonlinear case, Eq. (9), for the same set of parameters, as shown in Figs. 7(b), 7(d), and 7(f). We observe that for high amplitudes, both linear and nonlinear systems display a similar behavior, as can be seen by comparing Figs. 7(a) and 7(b) or Figs. 7(c) and 7(d). However, for low amplitudes of the non-Hermitian modulation, there is a qualitative difference between the linear and nonlinear systems, as shown in Fig. 7(e) and 7(f). Although a similar behavior is present near resonance, $\boldsymbol{\Delta q} \sim 0$, nonlinearity plays a stronger role, leading to the coexistence of different modes in a wider range of the parameter space.

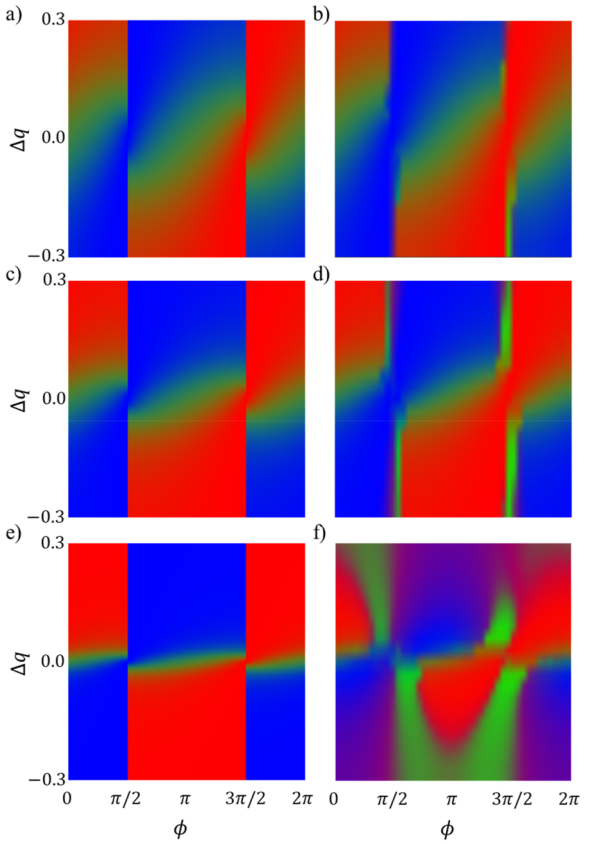

FIG. 7. Effect of the nonlinearity in the system. Comparison of the RGB image of the participations the first three transverse modes, H_0, H_1, and H_2 in the total field, in the parameter space of $(\phi, \Delta q)$ in the linear/nonlinear case, for (a) and (b) $((m_{re}, m_{im}) = 0.6$, (c) and (d) $((m_{re}, m_{im}) = 0.3$, and (e) and (f) $((m_{re}, m_{im}) = 0.1$. Other parameters used are $g = \alpha = 0.1$, $c = d = 1$.

APPENDIX C: BEAM SHAPING, ROBUSTNESS, AND EFFECTIVENESS

In addition to the mode-cleaning phenomenon, we also calculate the beam propagation, taking into account the modulation parameters that lay in the green and blue regions of Fig. 3(a). Figure 8 shows the beam propagation upon an input noisy beam for modulation parameter in the green region. We observe that the participations of all modes decrease while the H_1 and H_2 modes remain. Between these two, the H_1 mode is maximized with some participation of the H_2 mode, as shown in Fig. 8(a). The intensity profile evolution also shows how the beam profile changes along the propagation and converts into almost the H1 mode, as shown in Fig. 8(b).

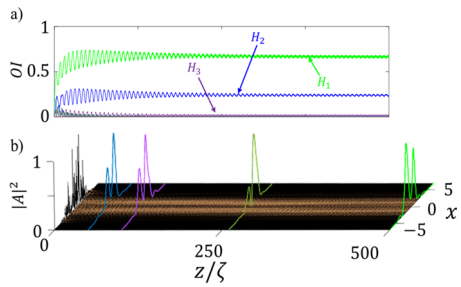

FIG. 8. (a) Relative mode intensity, *OI*, for an incident noisy beam, as a function of the propagation distance. (b) Evolution in the propagation of the corresponding profiles depicted at particular distances, namely, $z = 1\zeta, 50\zeta, 100\zeta, 260\zeta$, and 500ζ. The parameters used are $m_{re} = m_{im} = 0.6$, $Q = 0.975$, $\phi = 2.85$. Other parameters are same as those shown in Fig. 3.

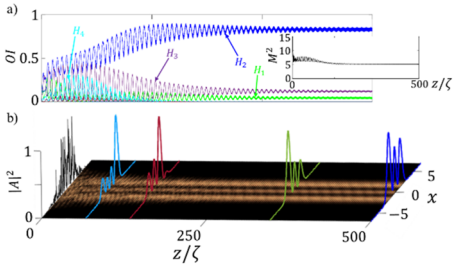

FIG. 9. (a) Relative mode intensity, *OI*, for an incident noisy beam, as a function of the propagation distance. The inset shows the evolution of the beam quality factor (M^2) in space. (b) Evolution in the propagation of the corresponding profiles depicted at particular distances, namely, $z = 1\zeta, 50\zeta, 100\zeta, 260\zeta$, and 500ζ. The parameters used are $m_{re} = m_{im} = 0.6$, $Q = 1.13$, $\phi = 1.85$. Other parameters are the same as those shown in Fig. 3.

The beam propagation for a point in the blue region of Fig. 3(a) is shown in Fig. 9. In this case, participation of the H_2 mode dominates as the beam propagates along the modulated waveguide, while very little percentage of the other mode remains, as can be seen in Fig. 9(a). The intensity profile propagation also shows that the output profile almost becomes the H_2 mode, as shown in Fig. 9(b). The inset of Fig. S.2a shows the evolution of the beam quality factor, M^2, where the M^2 value reaches at around 5, indicating the dominance of higher order modes, as we know that for lowest order mode, H_0, its value is 1.

Throughout this paper, all the studies have been performed considering a pure background parabolic potential where the modes are equidistant. In this section, we perform an analysis of the robustness of the proposed mechanism. In order to do that, we consider some perturbation form the pure parabolic potential, making the modes unequidistant. For this purpose, we deformed the potential from the pure parabolic case $V_0 = -cx^2$ to the more general case

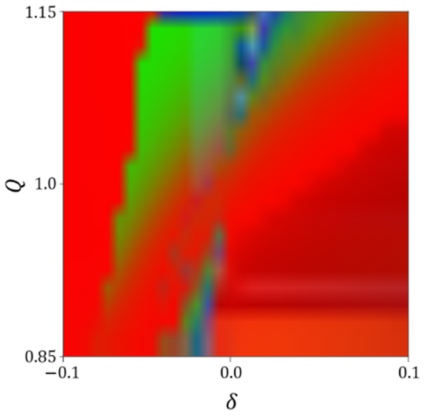

FIG. 10. Overlapped map of the normalized mode projections, *OI*, of all modes, in the total field in the parameter space (δ, Q), for a fixed value of the modulation amplitudes and spatial delay, where relative intensity of every mode corresponds to one color: red to H_0, green to H_1, blue to H_2, violet to H_3, cyan to H_4, brown to H_5, and black to the rest of modes. The parameters used are $m_{re} = m_{im} = 0.6$, $\phi = 4.42$, $g = \alpha = 0.1$, $c = d = 1$.

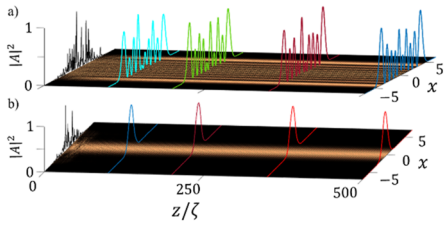

FIG. 11. Study of mode cleaning for a flat gain profile. Evolution in the propagation of the noisy beam with profiles depicted at particular distances, namely, $z = 1\zeta, 100\zeta, 220\zeta, 370\zeta$, and 500ζ for cases (a) without modulation and (b) with modulation. The parameters used are $m_{re} = m_{im} = 1.85$, $Q = 0.925$, $\phi = 4.42$, $g = 0$, $\alpha = 0.1$, $c = d = 1$.

$V' = -cx^2(1 \pm \delta x^2)$, where δ is a parameter controlling the deformation of the potential, which makes the modes unequidistant. We observe that the scheme is effective and mode-cleaning persists for small perturbations from the parabolic index profile. To perform this robustness analysis, we choose a point from the red region of Fig. 3(a), where the mode-cleaning phenomenon has been observed. So, we fix the spatial delay value at $\phi = 4.42$ and map the normalized mode projection of all the modes in the parameter space (δ, Q), as shown in Fig. 10. We see that the dominance of the red region in the parameter map means the mode-cleaning persists for the perturbed potential. By adjusting the modulation frequency, Q, corresponding to the deformation parameter, δ, it is possible to have the mode-cleaning phenomenon.

We also study the effectiveness of the mechanism for a flat gain profile of the waveguide. Till now, all the studies have been conducted considering a Gaussian gain profile with certain width, $p_0 e^{-gx^2}$, where $g = 0.1$. In this section, we examine whether this mode management technique is effective for a flat gain profile, which corresponds to $g = 0$. As an example, we consider the mode-cleaning effect for a flat gain profile. At first, we propagate a noisy input beam along the waveguide amplifier having a flat gain profile without any non-Hermitian modulation. We observe that the noisy beam remains as a multimodal beam as it propagates along the waveguide, as shown in Fig. 11(a). Next, we launch a noisy beam along the modulated waveguide and observe the propagation. We see that now the noisy beam converts into a bell-shaped Gaussian beam profile as it propagates along the longitudinal direction, as shown in Fig. 11(b). It should be noted that in this case of flat gain profile, we need much higher (nearly 3 times) amplitude of modulations than the previously observed mode-cleaning phenomenon with a Gaussian gain profile.

REFERENCES

[1] R. El-Ganainy, M. Khajavikhan, D. N. Christodoulides, and S. K. Ozdemir, "The dawn of non-Hermitian optics," Commun. Phys. **2**(1), 37 (2019).
[2] S. Longhi, "Parity-time symmetry meets photonics: A new twist in non-Hermitian optics," Europhys. Lett. **120**(6), 64001 (2017).
[3] A. Li, H. Wei, M. Cotrufo, W. Chen, S. Mann, X. Ni, B. Xu, J. Chen, J. Wang, S. Fan, C. Qiu, A. Alù, and L. Chen, "Exceptional points and non-Hermitian photonics at the nanoscale," Nat. Nanotechnol. **18**(7), 706–720 (2023).
[4] L. Feng, R. El-Ganainy, and L. Ge, "Non-Hermitian photonics based on parity–time symmetry," Nat. Photonics **11**(12), 752–762 (2017).

[5]W. W. Ahmed, R. Herrero, M. Botey, Z. Hayran, H. Kurt, and K. Staliunas, "Directionality fields generated by a local Hilbert transform," Phys. Rev. A **97**(3), 033824 (2018).
[6]W. W. Ahmed, R. Herrero, M. Botey, Y. Wu, and K. Staliunas, "Restricted Hilbert transform for non-Hermitian management of fields," Phys. Rev. Appl. **14**(4), 044010 (2020).
[7]S. B. Ivars, M. Botey, R. Herrero, and K. Staliunas, "Non-Hermitian control of optical turbulence in systems with fractional dispersion," Chaos, Solitons Fractals **165**, 112774 (2022).
[8]J. M. Pardell, R. Herrero, M. Botey, and K. Staliunas, "Non-Hermitian arrangement for stable semiconductor laser arrays," Opt. Express **29**(15), 23997–24009 (2021).
[9]C. Huang, F. Ye, and X. Chen, "Mode pairs in PT-symmetric multimode waveguides," Phys. Rev. A **90**(4), 043833 (2014).
[10]S. N. Ghosh and Y. D. Chong, "Exceptional points and asymmetric mode conversion in quasi-guided dual-mode optical waveguides," Sci. Rep. **6**(1), 19837 (2016).
[11]Q. Liu *et al.*, "Efficient mode transfer on a compact silicon chip by encircling moving exceptional points," Phys. Rev. Lett. **124**(15), 153903 (2020).
[12]S. Wu, W. Song, J. Sun, Z. Lin, H. Xin, S. Zhu, and T. Li, "Broadband asymmetric light transport in compact lithium niobate waveguides," Laser Photonics Rev. **17**(8), 2300306 (2023).
[13]V. A. Vysloukh and Y. V. Kartashov, "Resonant mode conversion in the waveguides with unbroken and broken PT symmetry," Opt. Lett. **39**(20), 5933–5936 (2014).
[14]D. Wang, Y. Wang, and L. Li, "Resonant mode conversion in partially parity-time-symmetric waveguides," Phys. Rev. A **109**(2), 023515 (2024).
[15]M. N. Akhter, S. B. Ivars, M. Botey, R. Herrero, and K. Staliunas, "Non-Hermitian mode cleaning in periodically modulated multimode fibers," Phys. Rev. Lett. **131**(4), 043604 (2023).
[16]M. N. Akhter, M. Botey, R. Herrero, and K. Staliunas, "Mode-cleaning in antisymmetrically modulated non-Hermitian waveguides," Nanophotonics **13**(7), 1017–1024 (2024).
[17]X. Zhu, A. Schülzgen, H. Li, H. Wei, J. V. Moloney, and N. Peyghambarian, "Coherent beam transformations using multimode waveguides," Opt. Express **18**(7), 7506–7520 (2010).
[18]F. M. Dickey and S. C. Holswade, "Beam shaping A review," in *Laser Beam Shaping Applications* (CRC Press, 2017), pp. 383–418.
[19]X. Tan, B.-Y. Gu, G.-Z. Yang, and B.-Z. Dong, "Diffractive phase elements for beam shaping: A new design method," Appl. Opt. **34**(8), 1314–1320 (1995).
[20]G. Zhou, X. Yuan, P. Dowd, Y. L. Lam, and Y. C. Chan, "Design of diffractive phase elements for beam shaping: Hybrid approach," J. Opt. Soc. Am. A **18**(4), 791–800 (2001).
[21]K. Staliunas, S. Longhi, and G. J. de Valcárcel, "Faraday patterns in low-dimensional Bose-Einstein condensates," Phys. Rev. A **70**(1), 011601 (2004).
[22]C. Tamm and C. O. Weiss, "Bistability and optical switching of spatial patterns in a laser," J. Opt. Soc. Am. B **7**(6), 1034–1038 (1990).
[23]K. Staliunas, M. F. H. Tarroja, and C. O. Weiss, "Transverse mode locking, antilocking and self-induced dynamics of class-B lasers," Opt. Commun. **102**(1–2), 69–75 (1993).
[24]Y. Yan and N. C. Giebink, "Passive PT symmetry in organic composite films via complex refractive index modulation," Adv. Opt. Mater. **2**(5), 423–427 (2014).
[25]Y. Jia, Y. Yan, S. V. Kesava, E. D. Gomez, and N. C. Giebink, "Passive parity-time symmetry in organic thin film waveguides," ACS Photonics **2**(2), 319–325 (2015).
[26]E. K. Keshmarzi, R. N. Tait, and P. Berini, "Spatially nonreciprocal Bragg gratings based on surface plasmons," Appl. Phys. Lett. **105**(19), 191110 (2014).
[27]F. Hindle, E. Fertein, C. Przygodzki *et al.*, "Inscription of long-period gratings in pure silica and germano-silicate fiber cores by femtosecond laser irradiation," IEEE Photonics Technol. Lett. **16**(8), 1861–1863 (2004).
[28]C. Hahn, E. K. Keshmarzi, S. H. Song, C. H. Oh, R. N. Tait, and P. Berini, "Unidirectional Bragg gratings using parity-time symmetry breaking in plasmonic systems," IEEE J. Sel. Top. Quantum Electron. **22**(5), 48–59 (2016).
[29]J. B. Lonzaga, S. M. Avanesyan, S. C. Langford, and J. T. Dickinson, "Color center formation in soda-lime glass with femtosecond laser pulses," J. Appl. Phys. **94**(7), 4332–4340 (2003).
[30]G. Cheng, L. Lin, K. Mishchik, and R. Stoian, "Polarization-dependent scattering of nanogratings in femtosecond laser photowritten waveguides in fused silica," Materials **15**(16), 5698 (2022).
[31]L. A. Fernandes, J. R. Grenier, P. R. Herman, J. S. Aitchison, and P. V. Marques, "Femtosecond laser fabrication of birefringent directional couplers as polarization beam splitters in fused silica," Opt. Express **19**(13), 11992–11999 (2011).